Transition of topological Hall effect for tetragonal Heusler Mn_2PtSn thin film

Satoshi Sugimoto,[1,*] Yukiko Takahashi,[1] and Shinya Kasai [1,2]

[1]*Research Center for Magnetic and Spintronic Materials, National Institute for Materials Science (NIMS), 1-2-1 Sengen, Tsukuba 305-0047, Japan*

[2]*JST, PRESTO, 4-1-8 Honcho, Kawaguchi, Saitama 332-0012, Japan*

Abstract

The large topological Hall effect is observed in Mn_2PtSn epitaxial thin films. Non-hysteretic topological Hall resistivity is attributed to the canted spins below the reorientation temperature, while the hysteretic topological resistivity at zero field vicinity captures the trend of antiskyrmion formation. A decrease in thickness enhances the contribution of dipolar interaction, leading to the additional antiskyrmion-type signal above the reorientation temperature. The amplitudes of these topological signals are strongly modulated by the film thickness, providing pathways for developing antiskyrmion hosting media via film engineering.

[*]Corresponding author: SUGIMOTO.Satoshi@nims.go.jp

Topological magnetic textures possessing the Berry curvature affect the electronic structure of the host material, leading to distinctive transport properties favorable for future high-performance spintronic devices. [1,2] The topological Hall effect (THE) is a transport property in which itinerant electrons are driven in the direction of the Hall effect. [3,4] The study of THE has been intrinsically linked to magnetic skyrmions, nanometric bubble domains in which intertwined wrapping spins result in a unit integer topological charge. [5] Magnetic skyrmions were initially discovered in non-centrosymmetric crystals with Dzyaloshinskii–Moriya interactions (DMI), [2,3,6,7] and further explored in centrosymmetric systems with frustrated magnetic exchange interactions. [8,9]

Of late, Mn-based tetragonal Heusler alloys have attracted attention as alternative skyrmion-hosting materials. Antiparticles of skyrmions, known as antiskyrmions (aSks), [10,11] were observed in $Mn_{1.4}Pt_{0.9}Pd_{0.1}Sn$ in a broader field and temperature range. [12] This compound belongs to the D_{2d} symmetry class, where in-plane anisotropic DMI cause the stability of the robust aSK phase [13]. Studies on analogous Heusler compounds reported so far include discussions on THE being linked to aSk stabilizations, for example, bulk Mn_2PtSn [14] and $Mn_{1.4}Pt_{1-y}Rh_ySn$. [15], and thin films of Mn_2PtSn [16], $Mn_{2-x}PtSn$ [17,18], and Mn_2RhSn. [19,20]. Note that for such anti(ferri)-magnetic materials with canted spin configurations, THE can arise in noncoplanar spin structures without links to skyrmions. [21,22,23] Vistoli et al. recently observed large THE in a canted antiferromagnet $Ca_{1-x}Ce_xMnO_3$, [24] and reported that non-“skyrmionic” bubble domains were responsible for THE due to the canted spin gradient [25]. For materials with canted spin configurations, the physical origin of THE needs to be carefully explored.

In this letter, we report the experimental observation of a large THE in a Heusler Mn_2PtSn epitaxial thin film over a wide range of temperatures, magnetic fields, and thicknesses. We propose a discussion that focuses on the hysteretic properties of THE and access the underlying magnetic structures.

Mn_2PtSn thin films (40 nm ~ 100 nm) were grown on MgO (001) substrates with a 20 nm thick MgO buffer layer, using dc magnetron sputtering from a $Mn_{50}Pt_{25}Sn_{25}$ alloy target. These films were deposited at ambient temperature and post-annealed at 500 °C for 30 min. The crystal structures of the Mn_2PtSn films were characterized using X-ray diffraction (XRD, Rigaku) with Cu-Kα radiation ($\lambda = 1.5406$ Å). Atomic-scale crystal structures were identified using transmission electron microscopy (TEM, FEI). Magnetization measurements were performed by a vibrating sample magnetometry technique using a magnetic property measurement system (MPMS, Quantum Design). The transport properties were measured by a four-probe method using a physical property measurement system (PPMS, Quantum Design). The variation in magnetic field between MPMS and PPMS is estimated below $\pm$ 0.1 mT.

The Mn_2PtSn tetragonal crystal structure is classified in the space group $I\bar{4}m2$, no. 119, as shown in Fig. 1(a). [16] The clear (110) and (220) peaks in the out-of-plane XRD spectra in Fig. 1(b) support the formation of this inverse Heusler compound. The cross-sectional TEM images in Fig. 1(c) capture the epitaxial growth of Mn_2PtSn crystals for all thicknesses from 40 nm to 100 nm. The sharp spotty patterns of the integrated nanobeam electron diffraction (NBDs), shown in Fig. 1(d), were also identified by the

$I\bar{4}m2$ symmetry. The lattice parameters are $a = 4.49 \pm 1$Å and $c = 6.08 \pm 2$Å for all thicknesses.

Figures 1(e) and (f) show the temperature dependences of longitudinal resistivity ρ_{xx} and magnetization M, respectively. The samples were field-cooled in a perpendicular field of 4 T to investigate saturated magnetization state. The kinks of ρ_{xx} and M mark the spin reorientation temperature T_{s} from the noncoplanar (NCP) ferrimagnet into coplanar (CP) ferrimagnets. [12] The Curie temperatures T_{c} are estimated as T_{c}~350 K from the gradient changes of M above room temperature.

The total Hall resistivity ρ_{xy} is composed of the ordinary Hall effect (OHE) ρ_{xy}^{OHE}, the anomalous Hall effect (AHE) ρ_{xy}^{AHE}, and additional THE ρ_{xy}^{THE}, as $\rho_{xy} = \rho_{xy}^{\mathrm{OHE}} + \rho_{xy}^{\mathrm{AHE}} + \rho_{xy}^{\mathrm{THE}}$. [2] The OHE is expressed as $\rho_{xy}^{\mathrm{OHE}} = R_0 H$ with Hall coefficient R_0. The AHE, dominated by intrinsic and side-jump scattering contributions [26,27], is rewritten as $\rho_{xy}^{\mathrm{AHE}} \sim S_{\mathrm{A}} \rho_{xx}^2 M$ with scaling coefficient S_{A}. Hence, the remaining THE contribution is simplified as follows.

$$\rho_{xy}^{\mathrm{THE}} = \rho_{xy} - R_0 H - S_{\mathrm{A}} \rho_{xx}^2 M. \quad (1)$$

In Fig. 2(a), the hysteresis curves of ρ_{xy}, ρ_{xx}, $\rho_{xy}^{\mathrm{OHE}} + \rho_{xy}^{\mathrm{AHE}}$, and ρ_{xy}^{THE} measured under a perpendicular field are plotted for a 40 nm thick sample at 150 K. The $\rho_{xy}^{\mathrm{OHE}} + \rho_{xy}^{\mathrm{AHE}}$ curve deviates from the ρ_{xy} curve below $H < 2$ T, with a clear emergence of THE. The ρ_{xy}^{THE} curve shows sign inversions between the positive and negative fields as a feature of the inversed topological flux. [17,28] We obtained the maximum THE signal as $\rho_{xy,\mathrm{max}}^{\mathrm{THE}} = 0.57$ $\mu\Omega$ cm for a 40 nm thick sample.

Nayak et al. reported that wide-field range THEs are primarily attributed to the noncoplanar canted spins in analogous ferrimagnetic compounds, [12,15] and

antiskyrmions should be linked at zero field vicinity, appearing as the hysteretic component of THE. To present the essence of these discussions, we introduce a process to separate the non-hysteretic and hysteretic topological contributions described below.

The non-hysteretic component of THE labeled as $\rho_{xy}^{\mathrm{tTHE}}$ can be extracted by adding ρ_{xy}^{THE} to change the field-sweep direction from $+4$ T to -4 T ($\rho_{xy,\mathrm{dec}}^{\mathrm{THE}}$) and change the field-sweep direction from -4 T to $+4$ T ($\rho_{xy,\mathrm{inc}}^{\mathrm{THE}}$), as follows.

$$\rho_{xy}^{\mathrm{tTHE}} = (\rho_{xy,\mathrm{dec}}^{\mathrm{THE}} + \rho_{xy,\mathrm{inc}}^{\mathrm{THE}})/2. \quad (2)$$

In addition, the hysteretic component ($\rho_{xy}^{\mathrm{hTHE}}$) can be calculated by making a difference as

$$\rho_{xy}^{\mathrm{hTHE}} = (\rho_{xy,\mathrm{dec}}^{\mathrm{THE}} - \rho_{xy,\mathrm{inc}}^{\mathrm{THE}})/2. \quad (3)$$

The quantifications of $\rho_{xy}^{\mathrm{tTHE}}$ and $\rho_{xy}^{\mathrm{hTHE}}$ are shown in Figs. 2(b), (d), and (f), for 40 nm thickness at 150 K and 50 K, and for 100 nm thickness at 50 K, respectively. All $\rho_{xy}^{\mathrm{tTHE}}$ show a similar trend as ρ_{xy}^{THE} shown in Figs. 2(a), (c), and (e). In Fig. 2(d), finite $\rho_{xy}^{\mathrm{hTHE}}$ appears as a positive peak signal near the zero field, corresponding to a converse hysteresis loop in the THE curve. At a converse hysteresis, the sign inversion of ρ_{xy}^{THE} occurs after H switches to the opposite direction. The sign of ρ_{xy}^{THE} is determined by the polarity of the topological charge $Q = mp = \pm 1$, which reflects the direction of out-of-plane magnetization $p = \pm 1$ and a structure parameter called the vorticity m. [2,29] The positive $\rho_{xy}^{\mathrm{hTHE}}$ indicates that Q will have same sign as H with wide-range hump-shaped features in $\rho_{xy}^{\mathrm{tTHE}}$. It is difficult to distinguish any topological domains from canted spins in such conditions, and we cannot insist on antiskyrmion formations only from these transport properties.

On the other hand, $\rho_{xy}^{\mathrm{hTHE}}$ shown in Fig. 2(d), obtained for a 100 nm thickness at 50 K, appears to be a negative dip $\rho_{xy}^{\mathrm{hTHE}} < 0$ as an inverse hysteresis in the THE loop.

In the same manner, this trend of $\rho_{xy}^{\mathrm{hTHE}}$ is considered to reflect the polarity inversion of Q. Since the field direction stays constant during this process, i.e., $p = const.$, the sign inversion of vorticity m is implied. Sivakumar et al. [20] reported such inversion of vorticity m without field switching indicated antiskyrmion formations, because the vorticity in antiskyrmions considers opposite sign as $m = -1$ to that of normal skyrmions as $m = +1$, [11,29,30]. Therefore, this negative $\rho_{xy}^{\mathrm{hTHE}}$ is considered to be a sufficient condition of antiskyrmion formations in Mn-based Heusler thin films. It should be noted that $\rho_{xy}^{\mathrm{hTHE}}$ does not represent THE itself induced by antiskyrmions. The total ρ_{xy}^{THE} in Fig. 2(e) shows asymmetric behavior with respect to field inversion due to the polarity switching.

The other notable features are emergences of zero magnetic field topological Hall signals in Figs. 2(d) and (f). The previous report of Mn_2PtSn thin film was focused on nonzero magnetic field THE, [16] where stabilizations of antiskyrmions were observed using direct imaging techniques. [12] In these reports, the helical magnetic phases were dominant at zero field vicinities, and THE associated with antiskyrmions were discussed mainly under finite field conditions. On the other hands, zero field topological Hall signals were also reported for the recent studies of thin film Mn_2RhSn [20] and Pd-doped $Mn_{1.5}PtSn$ [28] in conditions with low temperature range where relevant dipolar interaction increases. We next present systematic results of ρ_{xy}^{THE} and $\rho_{xy}^{\mathrm{hTHE}}$ for different temperature, field, and sample thickness to investigate the relation between antiskyrmion formations and thin film properties.

Figures 3(a) ~ (f) show the temperature and field dependences of $(\rho_{xy}^{\mathrm{tTHE}}, \rho_{xy}^{\mathrm{hTHE}})$ for 100 nm, 60 nm, and 40 nm thin films. The non-hysteretic $\rho_{xy}^{\mathrm{tTHE}}$ of

all thicknesses (Figs. 3(a), (c), and (e)) reproduces the bulk nature of ferrimagnetic Mn_xPtSn. [12,15] The large and constant THE signals appear below the spin reorientation temperature $T < T_s$, and immediately disappear above $T > T_s$. These steep changes in ρ_{xy}^{tTHE} in concert with the magnetic phase transition from the NCP to CP phases are common features of the canted spin textures of ferrimagnetic Mn_xPtSn, independent of any antiskyrmions.

On the other hand, the hysteretic ρ_{xy}^{hTHE} captures a trend of antiskyrmion formations, as discussed above, and can be modulated by film thickness. For the 100-nm-thick film shown in Fig. 3(b), the negative ρ_{xy}^{hTHE}, i.e., inverse hysteresis, appears below $T < T_s$. The absolute amplitude of ρ_{xy}^{hTHE} decreases with temperature and reaches zero around T_s. A small positive ρ_{xy}^{hTHE} remains above $T > T_s$ subsequentially. The finite ρ_{xy}^{hTHE} above T_s may be attributed to the pinned magnetic domains at zero field vicinity due to the crystal incompleteness.

For the thinner 60 nm film in Fig. 3(d), on the other hand, the positive ρ_{xy}^{hTHE} appears below $T < T_s$, and vanishes above $T > T_s$. This trend is similar to that of ρ_{xy}^{tTHE}, as the phase transition from the NCP phase to the CP phase without antiskyrmion formation.

For the thinnest 40 nm film shown in Fig. 3(f), the positive ρ_{xy}^{hTHE} appears below $T < T_s$ similarly to results of the 60 nm film. Additionally, antiskyrmion-type $\rho_{xy}^{hTHE} < 0$ is observed above $T > T_s$, where no antiskyrmion texture has been reported in bulk compounds. [15] The finite THE above T_s may be attributed to the additionally stabilized antiskyrmions for thin-film engineering, also reported for MnSi and FeGe compounds in cases of skyrmions. [31,32]

The modulation of $\rho_{xy}^{\mathrm{hTHE}}$ by film thickness feasibly reflects the variations in the dipolar energy, which plays a critical role in antiskyrmion formation. [33] Our 100 nm film is thick enough to reproduce the bulk nature, leading to antiskyrmion-type signals. The extension of antiskyrmion-type topological signal to zero field condition is considered due to decrease in perpendicular anisotropy in thin film samples, where the relevant dipolar energy will further increase from bulk samples. Once the thickness decreases, the net magnetization decreases and the contribution of dipolar energy becomes weaker, as is observed with the disappearance of negative $\rho_{xy}^{\mathrm{hTHE}}$ below 60 nm. Additionally, the formation of a metastable antiskyrmion phase at the limit of a weaker magnetic anisotropy was reported, [34] in which dipolar interactions are relatively dominant in domain formations. Such an energy limit is observed at a thickness of 40 nm above $T > T_{\mathrm{s}}$, where an increase in temperature promptly decreases the magnetic anisotropy, and the contribution of dipolar energy is dominant again.

Finally, we show the thickness dependences of the maximum THE amplitudes for non-hysteretic resistivity $\rho_{xy}^{\mathrm{tTHE}}\big|_{\mathrm{max}}$ and hysteretic resistivity $\rho_{xy}^{\mathrm{hTHE}}\big|_{\mathrm{max}}$, in Fig. 5(a) and Fig. 5(b), respectively. Notably, $\rho_{xy}^{\mathrm{tTHE}}\big|_{\mathrm{max}}$ increases from 100 nm to 40 nm below $T < T_{\mathrm{s}}$, from $0.1\ \mu\Omega\,\mathrm{cm}$ to $0.6\ \mu\Omega\,\mathrm{cm}$. Such a dependence of $\rho_{xy}^{\mathrm{tTHE}}\big|_{\mathrm{max}}$ is comparable with that seen in previous reports on Mn_2PtSn thin films. Thick epitaxial Mn_2PtSn film, i.e., close to the bulk condition, reported negligible THE, which may reflect the inherent crystal structure. [35]. The largest THE more than $0.5\ \mu\Omega\,\mathrm{cm}$ was reported for polycrystalline Mn_2PtSn crystal growth on thermally oxidized silicon, with the expectation of large defects and grains compared to epitaxial films. [16] Therefore, a

complete $I\bar{4}m2$ Mn_2PtSn thin film is considered to possess an inherently weak THE, and a decrease in thickness breaks the c-axis crystal symmetry and enhances the eventual THE. The thickness dependence of $\rho_{xy}^{\mathrm{tTHE}}\big|_{\mathrm{max}}$ above $T > T_{\mathrm{s}}$ appears to be complicated, showing weak but sign-inverted signals between 40 ~ 60 nm. We speculate incomplete coplanar spins above $T > T_{\mathrm{s}}$ may trigger such a non-systematic behavior for thinner film samples. The detail study of the magnetic structure will be required to access the origin of these anomalies.

The dependence of $\rho_{xy}^{\mathrm{hTHE}}\big|_{\mathrm{max}}$ is also clear in any temperature range. It shows a monotonic increase from 100 nm to 40 nm for $T < T_{\mathrm{s}}$ and decrease for $T > T_{\mathrm{s}}$, indicating the size and density of nontrivial spin textures, somewhen antiskyrmions, shows direct and systematic dependences on both thickness and temperature. The systematic variation of magnetic anisotropy of thin films is considered to play an essential role here. These results are examples of thin-film engineering to modulate THE, combined with stabilization of the antiskyrmion phase by tuning its dipolar energy.

In summary, we fabricated epitaxial tetragonal Heusler Mn_2PtSn thin films via magnetron sputtering and observed a large THE. The condition of antiskyrmion formations is systematically discussed in relation to the hysteretic properties of THE. Antiskyrmion-type signal was observed at zero field vicinity for the thickest 100 nm thin film at the noncoplanar ferrimagnetic phase. An additional antiskyrmion signal was obtained for the thinnest 40nm film above the reorientation temperature, which is unique to the thin film sample with weak magnetic anisotropy. These topological signals can be

systematically modulated by temperature and film thickness, providing a route to the realization of skyrmion-based spintronic devices.

ACKNOWLEDGEMENTS

This work was partially supported by the Japan Society for the Promotion of Science (JSPS) KAKENHI grant nos. JP20K14419, JP17K18892, JP18H03787, and JST, PRESTO grant no. JPMJPR18L3, Japan. The authors acknowledge W. Koshibae and X. Z. Yu for fruitful discussions.

DATA AVAILABILITY

The data that support the findings of this study are available within this article.

Figure Captions

FIG. 1. (a) Crystal structure of tetragonal Mn_2PtSn with $I\bar{4}m2$ space group. (b) X-ray diffraction pattern of 40 nm Mn_2PtSn thin film. (c) Cross-sectional transmission electron microscopy images of 100 nm and 40 nm Mn_2PtSn thin films. Positions of Mn, Pt, and Sn atoms are modeled with red, green, and blue colors, respectively. (d) Nanobeam electron diffraction pattern of 40 nm Mn_2PtSn thin film along [100] direction. (e) Temperature dependences of longitudinal resistivities of Mn_2PtSn. The spin reorientation temperatures T_s are indicated with dashed lines. (f) Temperature dependences of field-cooled magnetization of Mn_2PtSn at perpendicular fields of 4 T.

FIG. 2. Hysteresis loops of ρ_{xy} (black), ρ_{xx} (green), $\rho_{xy}^{\mathrm{OHE}} + \rho_{xy}^{\mathrm{AHE}}$ (red), and ρ_{xy}^{THE} (blue) of (a) 40 nm thick Mn_2PtSn at 150 K, (c) 40 nm thick Mn_2PtSn at 50 K, and (e) 100 nm thick Mn_2PtSn at 50 K, respectively. The closed (open) symbols indicate results for the field-sweep from $+4$ T to -4 T (-4 T to $+4$ T). Field dependences of $\rho_{xy}^{\mathrm{tTHE}}$ (black) and $\rho_{xy}^{\mathrm{hTHE}}$ (blue) of (b) 40 nm thick Mn_2PtSn at 150 K, (d) 40 nm thick Mn_2PtSn at 50 K, and (f) 100 nm thick Mn_2PtSn at 50 K, respectively.

FIG. 3. Temperature and field dependences of $\rho_{xy}^{\mathrm{tTHE}}$ and $\rho_{xy}^{\mathrm{hTHE}}$, for (a), (b) 100 nm thick Mn_2PtSn film, (c), (d) 60 nm thick Mn_2PtSn film, and (e), (f) 40 nm thick Mn_2PtSn film.

241 FIG. 4. Film thickness dependences of $\rho_{xy}^{\mathrm{tTHE}}\big|_{\mathrm{max}}$ and $\rho_{xy}^{\mathrm{hTHE}}\big|_{\mathrm{max}}$ obtained (a) below

242 spin reorientation temperature $T < T_{\mathrm{s}}$, and (b) above $T > T_{\mathrm{s}}$. The black and red dotted

243 lines indicate the increase in $\rho_{xy}^{\mathrm{tTHE}}\big|_{\mathrm{max}}$ and $\rho_{xy}^{\mathrm{hTHE}}\big|_{\mathrm{max}}$.

244

245

246

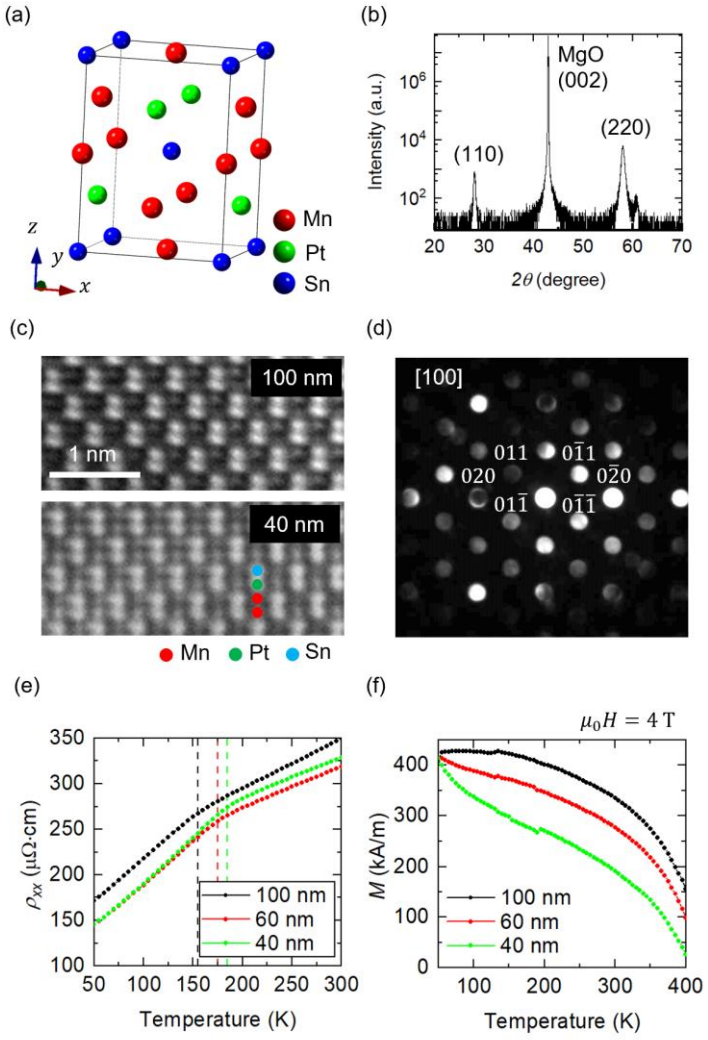

Fig. 1 Sugimoto *et al*.

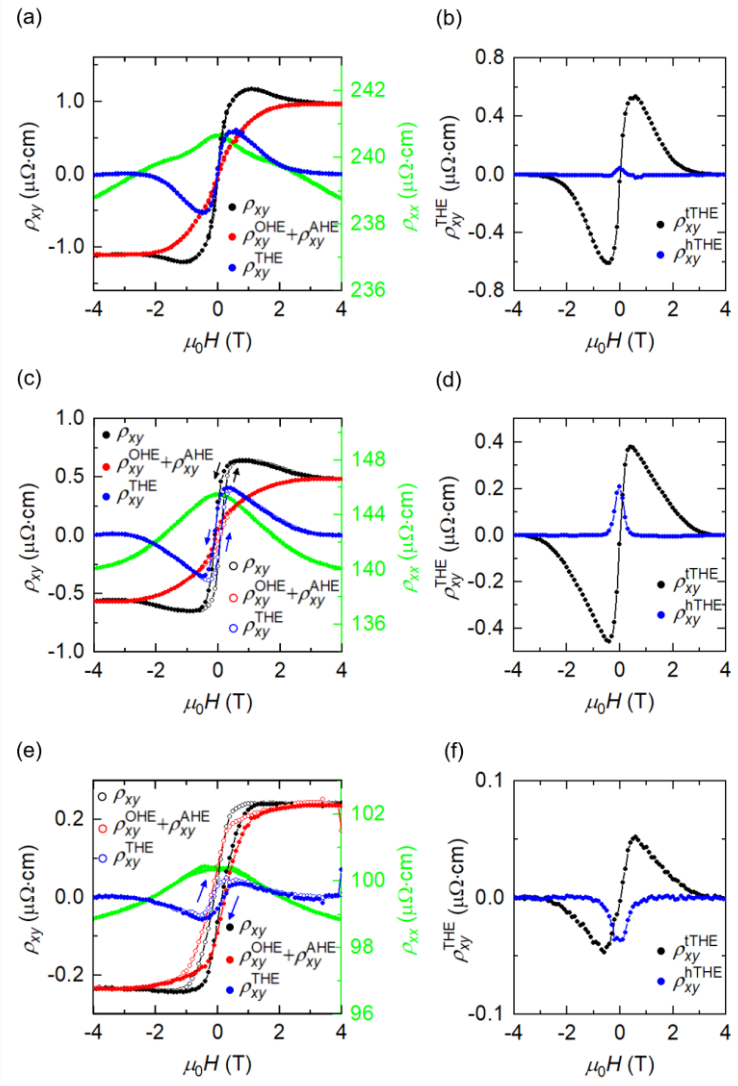

Fig. 2 Sugimoto *et al*.

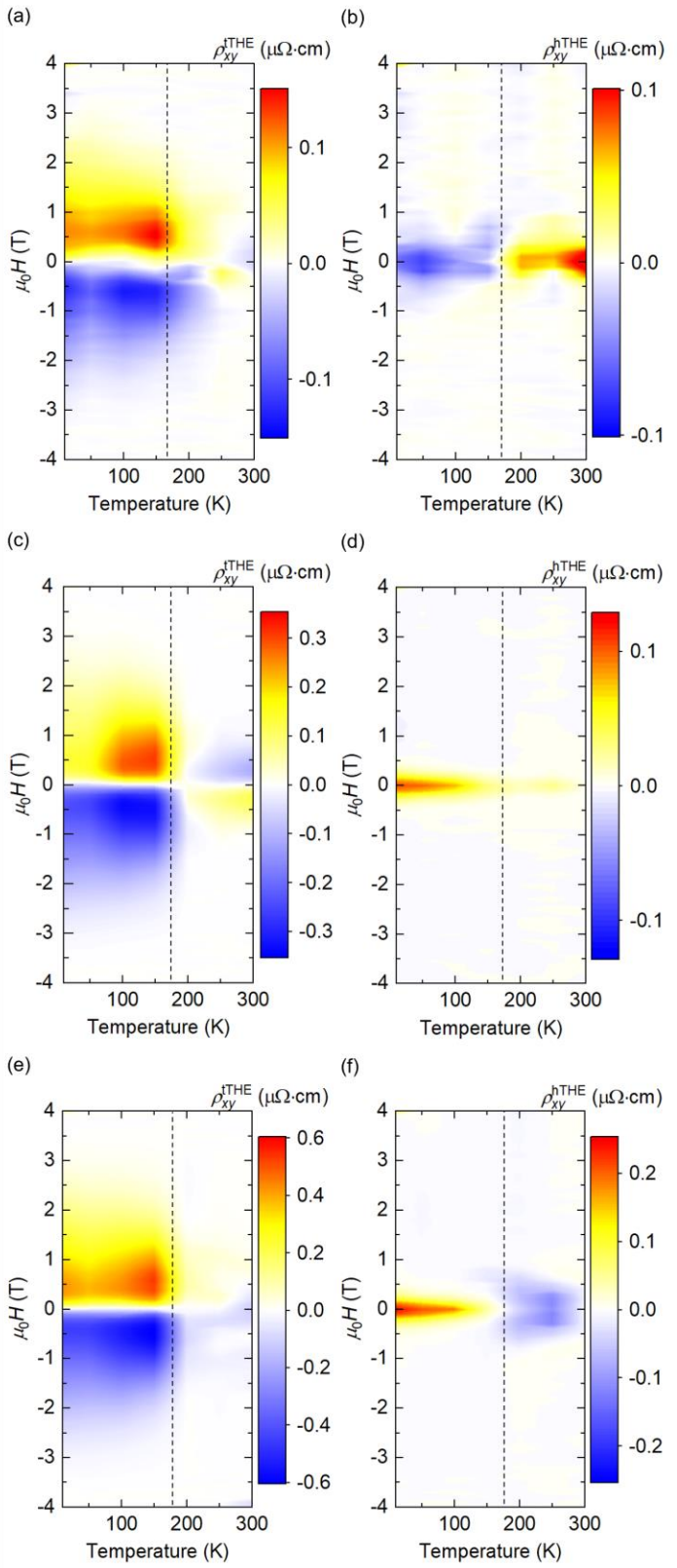

Fig. 3 Sugimoto *et al*.

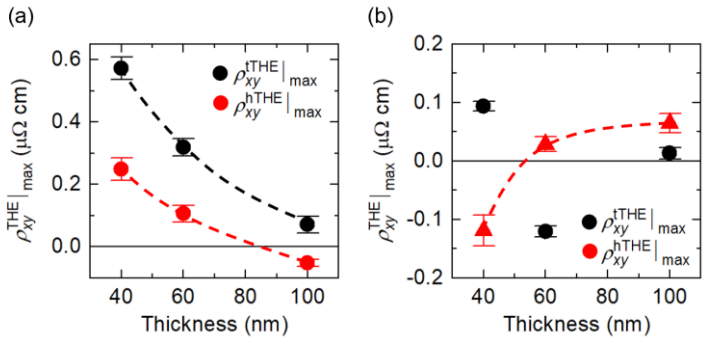

Fig. 4 Sugimoto *et al*.

262

1 F. Jonietz, S. Mühlbauer, C. Pfleiderer, A. Neubauer, W. Münzer, A. Bauer, T. Adams, R. Georgii, P. Böni, R. A. Duine, K. Everschor, M. Garst, and A. Rosch, Science **330**, 1648 (2010).

2 A. Neubauer, C. Pfleiderer, B. Binz, A. Rosch, R. Ritz, P. G. Niklowitz, and P. Böni, Phys. Rev. Lett. **102**, 186602 (2009).

3 N. Kanazawa, Y. Onose, T. Arima, D. Okuyama, K. Ohoyama, S. Wakimoto, K. Kakurai, S. Ishiwata, and Y. Tokura, Phys. Rev. Lett. **106**, 156603 (2011).

4 M. Onoda, G. Tatara, and N. Nagaosa, J. Phys. Soc. Jpn. **73**, 2624 (2004).

5 A. Fert, V. Cros, and J. Sampaio, Nat. Nanotechnol. **8**, 152 (2013).

6 S. Mühlbauer, B. Binz, F. Jonietz, C. Pfleiderer, A. Rosch, A. Neubauer, R. Georgii, and P. Böni, Science **323**, 915 (2009).

7 X. Z. Yu, N. Kanazawa, Y. Onose, K. Kimoto, W. Z. Zhang, S. Ishiwata, Y. Matsui, and Y. Tokura, Nat. Mater. **10**, 106 (2011).

8 S. Ishiwata, M. Tokunaga, Y. Kaneko, D. Okuyama, Y. Tokunaga, S. Wakimoto, K. Kakurai, T. Arima, Y. Taguchi, and Y. Tokura, Phys. Rev. B **84**, 054427 (2011).

9 S. Chakraverty, T. Matsuda, H. Wadati, J. Okamoto, Y. Yamasaki, H. Nakao, Y. Murakami, S. Shiwata, M. Kawasaki, and Y. Taguchi, Phys. Rev. B **88**, 220405 (2013).

10 A. N. Bogdanov, U. K. Rößler, M. Wolf, and K.-H. Müller, Phys. Rev. B **66**, 214410 (2002).

11 W. Koshibae and N. Nagaosa, Nat. Commun. **7**, 10542 (2016).

12 A. K. Nayak, V. Kumar, T. Ma, P. Werner, E. Pippel, R. Sahoo, F. Damay, U. K. Rößler, C. Felser, and S. S. P. Parkin, Nature (London) **548**, 561 (2017).

13 S. Huang, C. Zhou, G. Chen, H. Shen, A. K. Schmid, K. Liu, and Y. Wu, Phys. Rev. B **96**, 144412 (2017).

14 Z. H. Liu, A. Burigu, Y. J. Zhang, H. M. Jafri, X. Q. Ma, E. K. Liu, W. H. Wang, and G. H. Wu, Scr. Mater. **143**, 122 (2018).

15 V. Kumar, N. Kumar, M. Reehuis, J. Gayles, A. S. Sukhanov, A. Hoser, F. Damay, C. Shekhar, P. Adler, and C. Felser, Phys. Rev. B **101**, 014424 (2020).

16 Y. Li, B. Ding, X. Wang, H. Zhang, W. Wang, and Z. Liu, Appl. Phys. Lett. **113**, 062406 (2018).

17 P. Swekis, A. Markou, D. Kriegner, J. Gayles, R. Schlitz, W. Schnelle, S. T. B. Goennenwein, and C. Felser, Phys. Rev. Mater. **3**, 013001(R) (2019).

18 P. Swekis, J. Gayles, D. Kriegner, G. H. Fecher, Y. Sun, S. T. B. Goennenwein, C. Felser, and A. Markou, ACS Appl. Electron. Mater. **3**, 1323 (2021).

19 K. G. Rana, O. Meshcheriakova, J. Kübler, B. Ernst, J. Karel, R. Hillebrand, E. Pippel, P. Werner, A. K. Nayak, C. Felser, and S. S. P. Parkin, New J. Phys. **18**, 085007 (2016).

20 P. K. Sivakumar, B. Göbel, E. Lesne, A. Markou, J. Gidugu, J. M. Taylor, H. Deniz, J. Jena, C. Felser, I. Mertig, and S. S. P. Parkin, ACS Nano **14**, 13463 (2020).

21 Y. T. Y. Taguchi, Y. Oohara, H. Yoshizawa, N. Nagaosa, and Y. Tokura, Science **291**, 2573 (2001).

22 Y. Machida, S. Nakatsuji, Y. Maeno, T. Tayama, T. Sakakibara, and S. Onoda, Phys. Rev. Lett. **98**, 057203 (2007).

23 B. G. Ueland, C. F. Miclea, Y. Kato, A. Valenzuela, R. D. McDonald, R. Okazaki, P. H. Tobash, M. A. Torrez, F. Ronnig, R. Movshovich, Z. Fisk, E. D. Bauer, I. Martin, and J. D. Thompson, Nat. Commun. **3**, 1067 (2012).

24 L. Vistoli, W. Wang, A. Sander, Q. Zhu, B. Casals, R. Cichelero, A. Barthélémy, S. Fusil, G. Herranz, S. Valencia, R. Abrudan, E. Weschke, K. Nakazawa, H. Kohno, J. Santamaria, W. Wu, V. Garcia, and M. Bibes, Nat. Phys. **15**, 67 (2019).

25 J. J. Nakane, K. Nakazawa, and K. Nakazawa, Phys. Rev. B **101**, 174432 (2020).

26 N. Nagaosa, J. Sinova, S. Onoda, A. H. MacDonald, and N. P. Ong, Rev. Mod. Phys. **82**, 1539 (2010).

27 T. Miyasato, N. Abe, T. Fujii, A. Asamitsu, S. Onoda, Y. Onose, N. Nagaosa, and Y. Tokura, Phys. Rev. Lett. **99**, 086602 (2007).

28 V. Kumar, N. Kumar, M. Reehuis, J. Gayles, A. S. Sukhanov, A. Hoser, F. Damay, C. Shekhar, P. Adler, and C. Felser, Phys. Rev. B **101**, 014424 (2020).

29 N. Nagaosa, and Y. Tokura, Nat. Nanotechnol. **8**, 899 (2013).

30 A.A. Kovalev and S. Sandhoefner, Front. Phys. **6**, 98 (2018).

31 Y. F. Li, N. Kanazawa, X. Z. Yu, A. Tsukazaki, M. Kawasaki, M. Ichikawa, X. F. Jin, F. Kagawa, and Y. Tokura, Phys. Rev. Lett. **110**, 117202 (2013).

32 S. X. Huang and C. L. Chien, Phys. Rev. Lett. **108**, 267201 (2012).

33 K. Karube, L. Peng, J. Masell, X. Z. Yu, F. Kagawa, Y. Tokura, and Y. Taguchi, Nat Mater. **20**, 335 (2021).

34 M. Heigl, S. Koraltan, M. Vanatka, R. Kraft, and C. Abert, C. Vogler, A. Semisalova, P. Che, A. Ullrich, T. Schmidt, J. Hintermayr, D. Grundler, M. Farle, M. Urbánek, D. Suess, and M. Albrecht, Nat. Commun. **12**, 2611 (2021).

35 Y. Jin, S. Valloppilly, P. Kharel, J. Waybright, P. Lukashev, X. Z. Li, and D. J. Sellmyer, J. Appl. Phys. **124**, 103903 (2018).